Computers in Biology and Medicine 135 (2021) 104586

Contents lists available at ScienceDirect

Computers in Biology and Medicine

journal homepage: www.elsevier.com/locate/compbiomed

# Transient modelling of impact driven needle-free injectors

Yatish S. Rane, Jeremy O. Marston *

*Department of Chemical Engineering, Texas Tech University, Lubbock, TX, 79409, USA*

ARTICLE INFO

*Keywords:*
Injector
Simulation
Validation
Pressure impulse
Transient

ABSTRACT

Needle-free jet injectors (NFJIs) are one of the alternatives to hypodermic needles for transdermal drug delivery. These devices use a high-velocity jet stream to puncture the skin and deposit drugs in subcutaneous tissue. NFJIs typically exhibit two phases of jet injection – namely – an initial peak-pressure phase ($< 5$ ms), followed by a constant jet speed injection phase ($\gtrsim 5$ ms). In NFJIs, jet velocity and jet diameter are tailored to achieve the required penetration depth for a particular target tissue (e.g., intradermal, intramuscular, etc.). Jet diameter and jet velocity, together with the injectant volume, guide the design of the NFJI cartridge and thus the required driving pressure. For device manufacturers, it is important to rapidly and accurately estimate the cartridge pressure and jet velocities to ensure devices can achieve the correct operational conditions and reach the target tissue. And thus, we seek to understand how cartridge design and fluid properties affect the jet velocity and pressure profiles in this process. Starting with experimental plunger displacement data, transient numerical simulations were performed to study the jet velocity profile and stagnation pressure profile. We observe that fluid viscosity and cartridge-plunger friction are the two most important considerations in tailoring the cartridge geometry to achieve a given jet velocity. Using empirical correlations for the pressure loss for a given cartridge geometry, we extend the applicability of an existing mathematical approach to accurately predict the jet hydrodynamics. By studying a range of cartridge geometries such as asymmetric sigmoid contractions, we see that the power of actuation sources and nozzle geometry can be tailored to deliver drugs with different fluid viscosities to the intradermal region.

## 1. Introduction

Alternatives to using needles to deliver injectable drugs include novel drug delivery techniques such as needle-free jet injectors and dissolvable microneedles [1–4]. Needle-free jet injectors are among the many applications that use impulsive forces to create a high-velocity liquid jet. Pressurized air [5,6], compressed spring [7–9], and explosive charge [10,11] are some of the typically used actuation sources. The mechanical components needed for different actuation sources vary, which affects the injector design and cost. However, all the mentioned actuation sources create an initial high-pressure spike before the steady transfer of stored energy. There are two phases of impact-driven jet injections, i.e. initial peak-pressure phase (or start-up phase) and steady jet speed phase [9]. The initial high-pressure [6,12] ($\sim 10^7$ Pa) may adversely affect the device components and nozzle/cartridge, resulting in excessive wear and tear [13]. A peak pressure of this magnitude may also cause device slippage across the skin, causing displacement from the targeted delivery area, resulting in unsuccessful drug delivery.

Due to the increased tissue penetration depth, intra-muscular needle-free jet injectors require more power [14–16] than equivalent intra-dermal jet injectors and thus increased magnitude of initial peak pressure. Due to the peak over-pressure, both fluid and cartridge components (e.g. plunger tip) can compress and cause recoil, resulting in dramatic pressure fluctuations. In such cases, the pressure inside the cartridge can drop below the vapor pressure of the liquid, causing detrimental cavitation [17]. Additionally, the rapid expansion and collapse of the cavitation bubble results in regions of high-deformation rate inside the cartridge, which may damage the drug molecules in DNA or RNA vaccines. Therefore, it is essential to study the pressure and jet velocity profiles for various geometrical features over a range of fluid properties.

A needle-free jet injector device typically consists of two main components (as shown in Fig. 1) namely – 1) a reusable metal device that stores energy in various forms, and 2) a plastic cartridge/ampoule that holds the drug. Further, there are two classifications based on reusability of plastic cartridges such as 1) multi-use nozzle jet injector

* Corresponding author.
*E-mail address:* jeremy.marston@ttu.edu (J.O. Marston).

https://doi.org/10.1016/j.compbiomed.2021.104586
Received 26 February 2021; Received in revised form 1 June 2021; Accepted 12 June 2021
Available online 17 June 2021

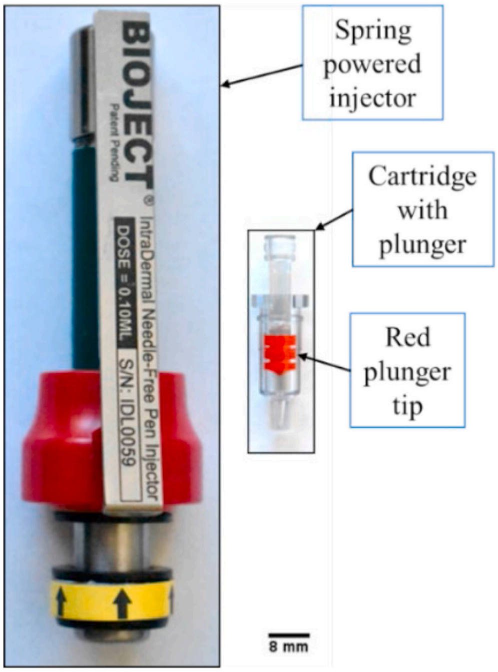


**Fig. 1.** Left image = Bioject® ID pen™ – Intra-Dermal spring-powered jet injector. Right image = ID pen™ disposable plastic cartridge with rubber plunger tip (red). Liquid filled cartridge is attached to bottom of the injector (Left image) to create a jet.

(MUNJI) [18–20] and 2) disposable cartridge jet injector (DCJI) [18]. It has been reported [18,19] that reusable plastic cartridges cause cross-contamination between patients and hence only disposable plastic cartridges (DCJI) are now used. Manufacturing techniques such as injection molding allows us to reduce the cost of DCJI plastic cartridge production significantly once an efficient cartridge geometry is achieved, which is especially economically attractive [21] for mass vaccinations. As such, tailoring cartridge geometry according to fluid and device properties is paramount and allows us to use the same metal device for multiple drugs.

Understanding the fluid properties and desired penetration depth of the drug are the minimum pre-requisites to computing the required jet velocity profile and, in turn, the required driving pressure and cartridge design to achieve the desired outcome. Previous work [7,9,12,22] suggests that the pressure and jet velocity profile vary with liquid viscosity, compressibility, and device characteristics; as such, there is a need to develop a model to accurately predict the pressure profile for a given combination of cartridge geometry and fluid properties.

There have been several experimental [9,23,24] and modelling [22,25,26] efforts to understand different phases of jet injection and develop predictive models. One recent numerical modelling study [25] showed the effect of conical cartridge geometrical parameters on peak pressure and jet velocity. However, rheological parameter variation was not covered. Experimental studies [27,28] have shown that increasing orifice diameter decreases the upstream cartridge pressure, but increases the penetration depth inside the tissue, based upon jet power considerations. These studies also show that the cartridge pressure during the steady jet speed phase changes with the peak pressure and are directly correlated to each other. Therefore, an increase in the orifice diameter offers a simple way to reduce the peak pressure for any cartridge geometry, assuming that increase in tissue penetration depth is acceptable.

In previous computational fluid dynamics (CFD) work [7], we performed the optimization of cartridge geometries for a range of rheological parameters. It also asserts that jet penetration depth in tissue can be controlled by changing cartridge geometry. The prediction of transient pressure and jet velocity profiles using CFD technique has been reported in literature [6,22,25], whilst an analytical model [1,18,19] consisting of partial differential equations (PDEs) can be used as a simple predictive model to estimate the behavior of the jet during an injection process. Here, the principle objective is to provide insight into some subtle transient features that can be resolved with CFD simulations and used to improve the predictive capabilities of the simpler mathematical model to estimate the pressure and velocity profiles of jet injection. The broader motivation behind this objective is to provide a facile method to tailor cartridge geometry to a specific fluid rheology.

## 2. Methods

In the present study, we use two different methodologies to estimate cartridge pressure and jet velocity profiles. The first methodology involves the transient CFD analysis, where the experimentally observed plunger displacement profile is used as an input for the simulation (to provide the translation of the rear wall) and calculate upstream cartridge pressure profile. The second methodology involves the transient predictive model, where the previously used Baker and Sanders approach [12] is modified using the characteristic curves of Euler

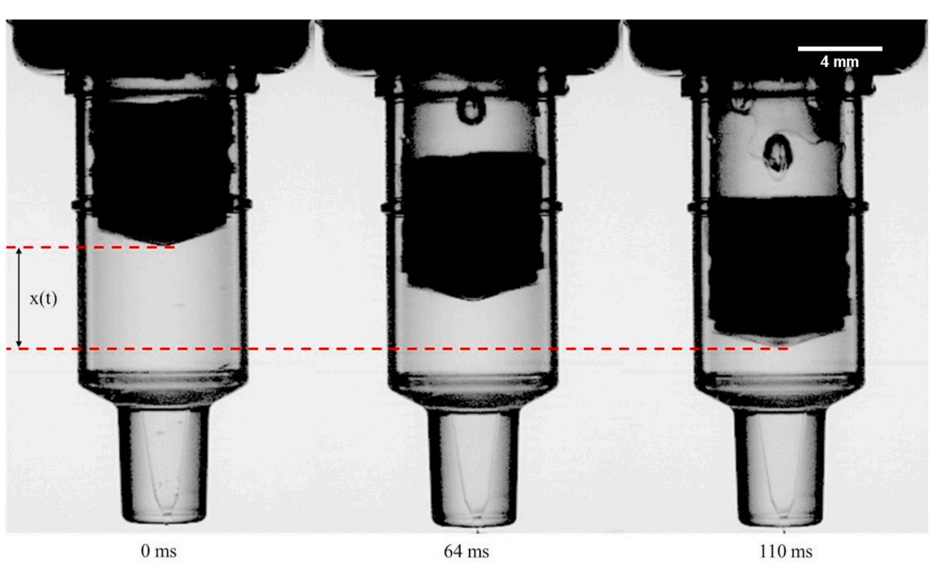


**Fig. 2.** Time sequence of snapshots for jet injection of glycerine using ID pen. x(t) represents the plunger displacement, x at time, t.

**Table 1**
Compressibility data required to model compressible liquid using the Tait equation of state under isothermal conditions. Values of given parameters for these two liquids are taken from ANSYS Fluent Material Database.

| Liquid name | Density exponent ($n$) | Reference Bulk Modulus ($B_0$) (pa) | Reference Density ($\rho_0$) (at $p_0 = 1$atm) (kg/m$^3$) | Viscosity (Pa.s) |
|---|---|---|---|---|
| Water | 7.15 | 2.2e+09 | 998.2 | 0.001 |
| Glycerine | 7 | 4.35e+09 | 1259.9 | 0.799 |

number ($Eu$) versus Reynolds number ($Re$) to include the effect of cartridge geometry and fluid rheology. The characteristic curves of $Eu$ based on $Re$ are calculated using steady-state CFD simulations for each cartridge geometry. The transient predictive model is then validated using the pressure data calculated from the transient CFD analysis and the experimentally observed plunger displacement profiles.

### 2.1. Experimental setup

Fig. 1 shows the spring-powered jet injector device used in this study. The plastic (polycarbonate) cartridge in Fig. 1 is designed to deliver 0.1 ml in the intradermal region of the skin. In our experimental setup, we recorded the plunger movement inside the cartridge using a high-speed video camera (Phantom V1611 - Vision Research) at a frame rate of 30000 fps. By performing frame-by-frame analysis of the videos (as per Fig. 2), we calculate the plunger displacement profiles and estimate the jet speed profile. Here, to study the behaviour of jet injectors at extremes of fluid properties, we used two Newtonian liquids: water (ultrapure milliQ) and glycerine (Macron Fine Chemicals).

The initial peak-pressure ($\sim 10^6$ Pa) [9,23,27] is strong enough to shake the entire jet injector assembly and therefore the jet injector is fixed onto an opto-mechanic rail system at the time of injection. To further reduce error in plunger displacement, we also log the shaking of jet injector using a multi-point tracking method and subtract it from plunger displacement profile as shown in our previous work [9]. Video analysis for plunger movement tracking is performed in MATLAB and the plunger displacement profile is given as an input in ANSYS Fluent for transient CFD analysis.

### 2.2. Numerical simulations (CFD) analysis

Numerical simulations are performed in ANSYS Fluent (v18.2), which uses finite volume analysis to numerically solve the fundamental governing equations (equation (1)) – namely – the continuity equation for mass balance and Navier-Stokes equation for momentum balance.

$$\frac{\partial \rho}{\partial t} + \underline{\nabla} \cdot \rho \underline{u} = 0, \quad \rho\left(\frac{\partial \underline{u}}{\partial t} + \underline{u} \cdot \underline{\nabla}\, \underline{u}\right) = -\underline{\nabla} p + \underline{\nabla} \cdot \underline{\underline{\sigma}} \tag{1}$$

Where, $t$ represents time, $\rho$ is fluid density, $p$ is pressure, $\underline{u}$ is a velocity vector and $\underline{\underline{\sigma}}$ is the stress tensor. 2-D axisymmetric simulations are performed to minimize the computational load without compromising accuracy of the results. The input for simulation (experimental plunger displacement) is modified such that it is smooth in the steady jet speed phase, which also improves the computational efficiency (see supplementary info).

The present study involves two types of CFD analysis, 1) transient CFD analysis, where the experimental plunger displacement profiles (Fig. 6(a)) are used to calculate corresponding cartridge pressure profiles (Fig. 6(b)) and, 2) steady-state CFD analysis, where the pressure drop across a cartridge geometry is estimated at a given flow rate, and characteristic curves of Euler number versus Reynolds number are calculated for each cartridge geometry (Figs. 9 and 12).

In our transient CFD analysis, the initial oscillations in start-up phase can be estimated using compressibility properties of liquids. ANSYS Fluent utilizes the Tait equation of state (equation (2)) to model compressible liquids, which demonstrates a nonlinear relation between pressure and density under isothermal conditions. The compressibility data for water and glycerol is given in Table 1. The Tait equation of state can be given as follows [10]:

$$\left(\frac{\rho}{\rho_0}\right)^n = \frac{B}{B_0} = \frac{B_0 + n(p - p_0)}{B_0} \tag{2}$$

Where, $n$ is the density exponent, $\rho$ & $B$ are liquid density and bulk modulus respectively at cartridge pressure $p$, and $\rho_0$ & $B_0$ are liquid density and bulk modulus at reference pressure $p_0$ (1 atm).

For high viscosity liquids [7], laminar conditions are implemented whereas turbulent flow for low viscosity liquids is modelled using the standard k-ε model. Simulations are performed under isothermal conditions and gravitational forces are neglected. Dynamic meshing is implemented to update the mesh at each time step and maintain optimal mesh density to balance the result accuracy and the computational load.

As per Fig. 3, the mesh density gradually increases from the moving plunger (A) to the cartridge outlet (D). Higher mesh density at the cartridge outlet is required to accurately estimate the turbulence losses in high Reynolds number flows. The mesh is optimized such that the residual error of at most $10^{-6}$ is achieved for all the velocity components and continuity equation throughout the injection timeframe. In our optimized mesh, we increased the mesh density from ~22 mesh points/mm in the upstream cartridge region to ~630 mesh points/mm in the nozzle exit region (as shown in Fig. 3). Adaptive time stepping feature in ANSYS Fluent is used to reduce the computational load in modelling the

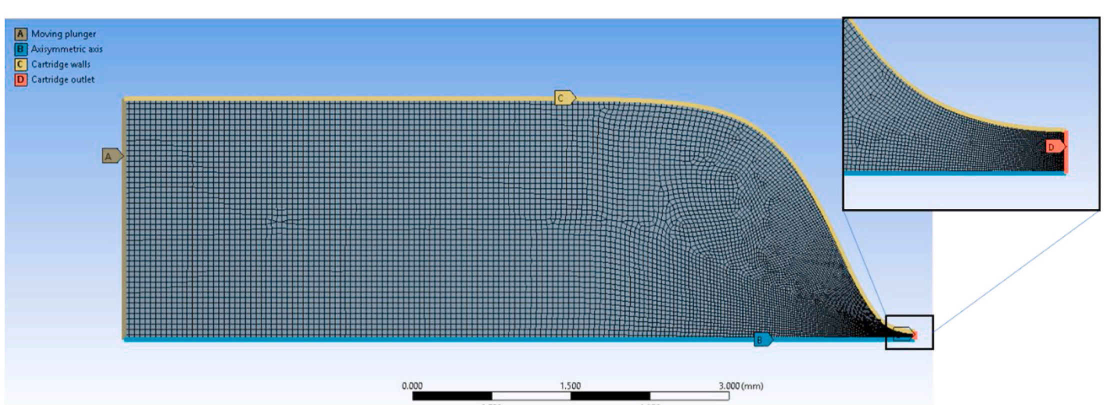


**Fig. 3.** Visual representation of gradient meshing for a cartridge geometry derived from Richard's function. Moving plunger wall only applies to transient CFD analysis, which uses ID pen cartridge geometry in Fig. 4(a).

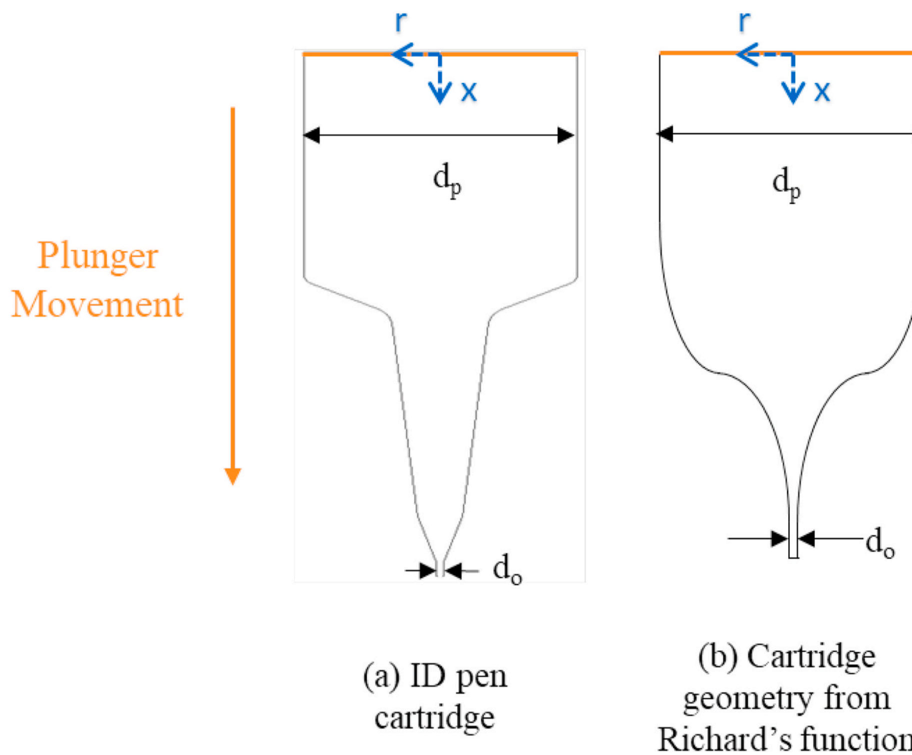


**Fig. 4.** Both the cartridge geometries are used in steady-state CFD simulations to develop geometry-specific *Eu* vs. Re correlations. Transient CFD analysis uses an experimental plunger displacement profile (ID pen geometry) as an input to calculate pressure losses. Reproduced, with permission, from Journal of Controlled Release, 319, Rane Y., Marston J., Computational study of fluid flow in tapered orifices for needle-free injectors, 382–396, Copyright Elsevier (2020). See Ref. 3.

start-up phase as shown in Fig. 6(a). Here, we use similar mesh optimization methodology for the transient CFD analysis and the steady-state CFD simulations. Furthermore, for transient CFD analysis, we conducted a time resolution optimization to yield a maximum time step of 80 microseconds, which satisfies the CFL (Courant, Friedrichs, and Lewy) condition, commonly used in transient CFD simulations. Additional information about the experimental validation of transient CFD analysis can be found in the supplementary information. In our previous work, we perform an extensive experimental validation of steady-state CFD simulations [7].

Both the cartridge geometries in Fig. 4(a) & (b) are used in steady-state CFD simulations. However, transient CFD analysis is only performed with the ID pen cartridge geometry because it requires the experimental plunger displacement as an input. Fig. 4(b) shows a sigmoidal cartridge geometry generated using Richard's function [7], given as:

$$d(x) = \frac{d_p - d_o}{\left(1 + (\delta - 1)^* e^{-k^*(x - x_0)}\right)^{\frac{1}{\delta - 1}}} + d_o \tag{3}$$

Where, $\delta$ and $k$ determine the inflection point in the radial direction and the slope of taper respectively, whilst *d(x)* gives the outline of cartridge geometry, and $x_o$ dictates the inflection point in the axial direction. $d_p$ is plunger diameter (or upstream cartridge inner diameter) and $d_o$ is orifice diameter (as per Fig. 4).

Here, the transient CFD analysis requires experimental plunger displacement profile as an input to estimate the pressure losses for ID pen cartridge geometry. Additionally, transient CFD analysis requires significant computational power (~24–48 h with four 3.6 GHz processors) for meshing and for solving the governing equations over the fluid domain (equation (1)) to estimate the velocity and pressure fields. Therefore, it is beneficial to develop a predictive tool, which requires significantly less computational time/power to estimate jet velocity and pressure losses for a given cartridge geometry. Here, we modify the previously used approach (a set of PDEs – equations (4) and (5) – from Baker and Sanders [12]) to develop transient predictive model, which requires significantly less computational power (~5 min with four 3.6 GHz processors).

### 2.3. Transient predictive model

To expand the applicability of numerical simulations results, we can develop an accurate predictive model using the dimensionless relationship between pressure loss and flow rate. In the literature [12,24,29], there are many variations of models to characterize impact-driven jet injectors but the underlying set of partial differential equations (PDEs) are derived from a similar force balance. Here, we modify the existing mathematical model [12,23] to include variation in the fluid rheology and cartridge geometry. We propose a model that considers cartridge geometry and viscous and turbulent losses.

The force balance for spring-powered jet injectors is performed at the plunger tip, which gives rise to the set of PDEs as follows [12,23,24]:

$$\frac{dp(t)}{dt} = \frac{(B + p(t))\frac{dx(t)}{dt} - \frac{BA_o}{A_p}v_j(t)}{L - x(t)} \tag{4}$$

$$\frac{d^2x(t)}{dt^2} = \frac{k_s(x_c - x(t))}{m_p} - \frac{A_p p(t)}{m_p} - \frac{dx(t)}{dt}\frac{f_p(t)}{m_p\left|\frac{dx(t)}{dt}\right|} \tag{5}$$

In equation (4), $B$ is the bulk modulus of the fluid, $L$ is the total plunger displacement during jet injection, $A_p$ and $A_o$ are the cross-sectional areas of the plunger (or the upstream cartridge) and orifice respectively, *p(t)* is the cartridge pressure profile, *x(t)* is the plunger displacement profile, and $v_j(t)$ is the jet velocity profile. Equation (4) relates the pressure and velocity fields in the cartridge using continuum analysis and the definition of bulk modulus.

In equation (5), $k_s$ is the spring constant, $x_c$ is spring compression length at the start of injection, $m_p$ is mass of the plunger, $f_p$ is the frictional force caused due to rubber plunger tip. Some of the key

**Table 2**
Bioject® ID pen™ device specifications and cartridge dimensions for both the geometries in Fig. 4.

| $k_s$ (N/m) | $m_p$ (g) | $x_c$ (mm) | $d_p$ (mm) | $d_o$ (μm) | $L$ (mm) |
|---|---|---|---|---|---|
| 12137 | 80 | 45 | 4.57 | 155 | 6.1 |

parameters pertaining to the certridge geometry are listed in Table 2. Equation (5) gives the force balance between acting spring force and opposing fluid, frictional forces. The set of PDEs were iteratively solved in MATLAB using 'ode45' solver.

The frictional force ($f_p$) can be broken down into two parts – namely – 1) resistance due to the flow of a thin fluid film which is generated in the clearance gap between the plunger tip and the interior of the cartridge and 2) friction from contact between the plunger and cartridge barrel. The frictional force can be derived using the principles of tribology, and the coefficient of friction has been accurately modelled in the literature [5,6,23,25]. Here, we use existing equations for plunger frictional force, which can be given as below:

$$f_p(t) = p_{ps}(t)\ (\pi d_p h) + \alpha\ (p_c + p_{ps}(t))\ (\pi d_p b) \tag{6}$$

$$p_{ps}(t) = p(t) + \frac{3}{2}\frac{\mu v_p(t) d}{h^2} \tag{7}$$

Where, $p_{ps}$ is the average compressive force on the plunger seal, $d_p$ is plunger diameter (or cartridge inner diameter), $h$ (= 0.05 mm) is clearance gap, $\alpha$ is the coefficient of friction between the rubber plunger tip and the interior wall of the polycarbonate cartridge [25], $p_c$ (= 3.5 MPa) [23] is initial compression force on the plunger tip due to press-fit in the cartridge, $b$ (= 4.2 mm) is the contact width (section of the plunger tip touching the cartridge wall, as per Fig. 5), $\mu$ is fluid viscosity, $v_p(t)$ is the plunger velocity and, $d$ (= 1.5 mm) is the diameter of ring section of the plunger tip (as per Fig. 5).

Navier-Stokes and continuity equations [7], which are used for momentum and mass conservation respectively, are solved over a given fluid domain to estimate velocity and pressure fields in the system. In the absence of direct analytical solution to these equations, empirical correlations and friction factor charts are typically used to approximately calculate the pressure losses in fluid flow. Previous studies [23,24] have used friction factor charts and empirical hydraulic loss correlations (in set of PDEs, equations (4) and (5)) to consider the effects of cartridge geometry on pressure losses and jet velocity. However, it is limited to linear tapered or step gradient nozzles/cartridges and does not consider a wide range of Reynolds numbers.

Here, we use the correlations between Euler number ($Eu$) and Reynolds number ($Re$) (equation (9)) to estimate the viscous and turbulent fluid flow losses. As mentioned in Section 2.2, steady-state CFD simulations were performed over a range of cartridge geometries and fluid viscosities to obtain the geometry-specific correlations of Euler number ($Eu = \frac{p}{0.5\rho v_j^2}$) versus Reynolds number ($Re = \frac{\rho v_j d_o}{\mu}$). In the present study, the use of an Euler number considers both the wide variation in cartridge geometry and Reynolds number. The jet velocity ($v_j(t)$) term in equation (4) facilitates the inclusion of Euler number in the set of governing PDEs for transient predictive model. The fluid velocity at the orifice, i.e. jet velocity, can be expressed as:

$$v_j(t) = \sqrt{\frac{2p(t)}{\rho^* Eu}} \tag{8}$$

Where, Euler number, $Eu = f(Re)$, $\rho$ is liquid density, $p(t)$ and $v_j(t)$ are the upstream cartridge pressure and jet velocity at time $t$.

## 3. Results and discussions

### 3.1. Transient CFD analysis

The accuracy of numerical simulations depends upon several parameters such as mesh density, solver type, initial guess values, and residual error. Section 2.2 and supplementary information details the procedures used for the validation of results in transient CFD analysis.

Here, Fig. 6(a) shows the experimentally observed plunger displacement profiles for 10 repeat trials. After the start-up phase ends (~5 ms), plunger displacement profiles follow an approximately constant slope, yielding constant jet velocity throughout the jet injection. In Fig. 6(a), we see that completion of glycerine injection takes more than double the time required for water injection. For the same cartridge geometry and injector device, plunger velocity for glycerine (~75 mm/s) is significantly slower than in case for water (~160 mm/s). Thus, jet velocities for these two liquid are different ($(v_j)_{\text{glycerine}} \sim 63$ m/s, $(v_j)_{\text{water}} \sim 134$ m/s), which ultimately affects the jet penetration depth [27,30] inside the tissue.

Utilizing an experimental plunger displacement profile as an input to the transient CFD analysis, we calculate the pressure profile for above two liquids as shown in Fig. 6(b). We can see that jet injection of glycerine shows higher overall pressure profile than that of water. Although the driving pressure is approximately 3 times higher for glycerine, jet velocity (~63 m/s) is significantly lower (~52%) due to significant viscous losses in laminar flow regime at the orifice region.

In Fig. 6(b), we also see that there is a second pressure peak around 3 ms for both the fluids. Figure C in the supplementary info shows us that there are two peaks in plunger velocity for these two fluids. The initial peak around 0.5 ms is due to the initial spring impact on the plunger, which results in the initial peak pressure in Fig. 6(b). The second peak around 3 ms marks the end of initial oscillations in the start-up phase, this generates the second peak pressure for both fluids, as seen in Fig. 6 (b). The initial spring impact causes compression of the plunger tip followed by the slight relaxation of plunger tip. This second peak in the plunger velocity profile can be attributed to the plunger slippage due to the plunger tip relaxation. Additionally, we see in figure C of supplementary information that water shows the higher peak plunger velocity magnitude for these two peaks than glycerine. This can be attributed to the higher bulk modulus (or lower compressibility) value of glycerine than water, and thus glycerine resists the change in plunger

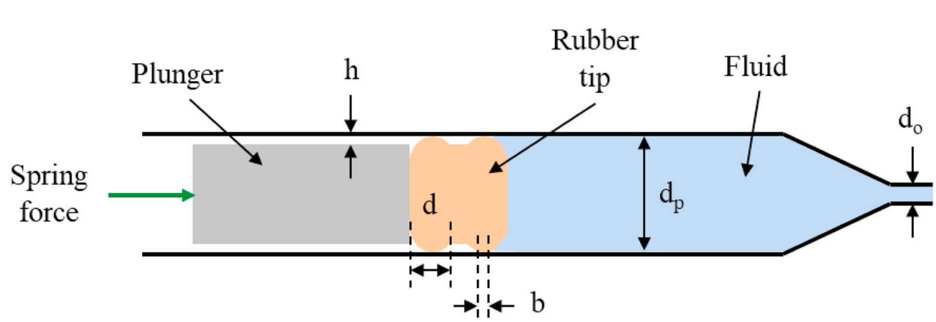


**Fig. 5.** Schematic of needle free jet injector cartridge and plunger with variables defined in the main text. (Not to scale).

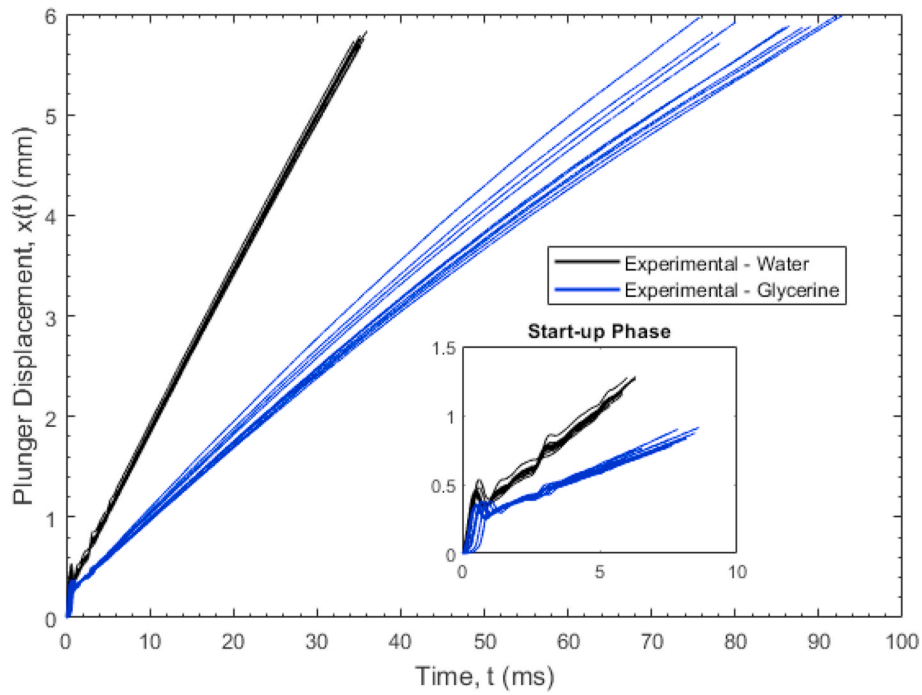


(a)

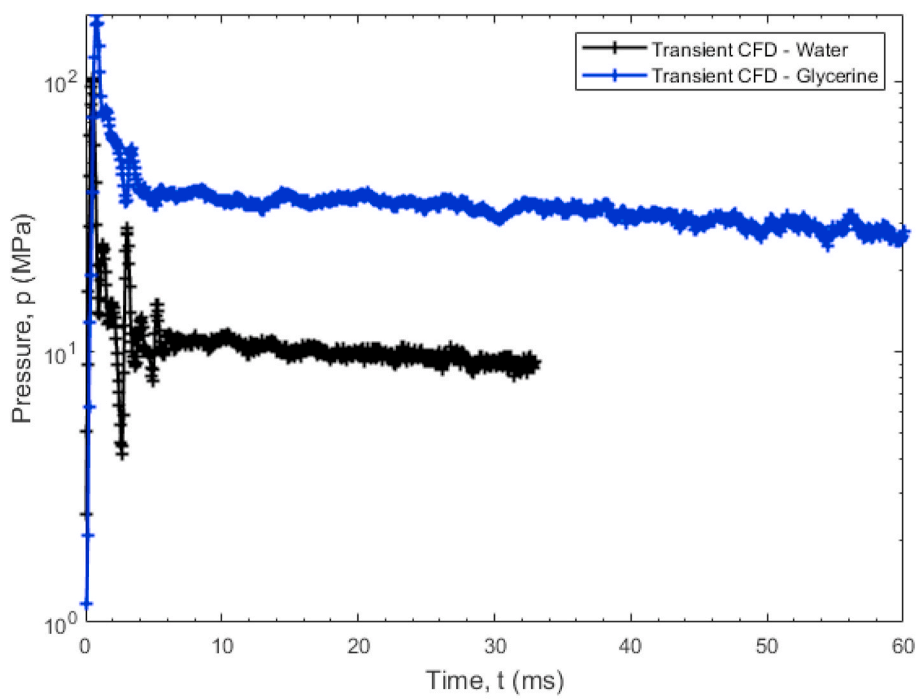


(b)

**Fig. 6.** (a) Experimental plunger displacement (x) with respect to time (t) for ID pen jet injections of water and glycerine. 10 trials for each fluid. Calculated from high-speed video as shown in Fig. 2. Sub-plot shows start-up phase of jet injection. (b) Pressure profile generated with transient CFD analysis, where experimental plunger displacement profile is used as an input.

displacement, which results in a lower magnitude of peak plunger velocity for glycerine.

### 3.2. *Transient predictive model*

In the present work, the set of partial differential equations (equations (4) and (5)) are solved with a fourth order Runge-Kutta method

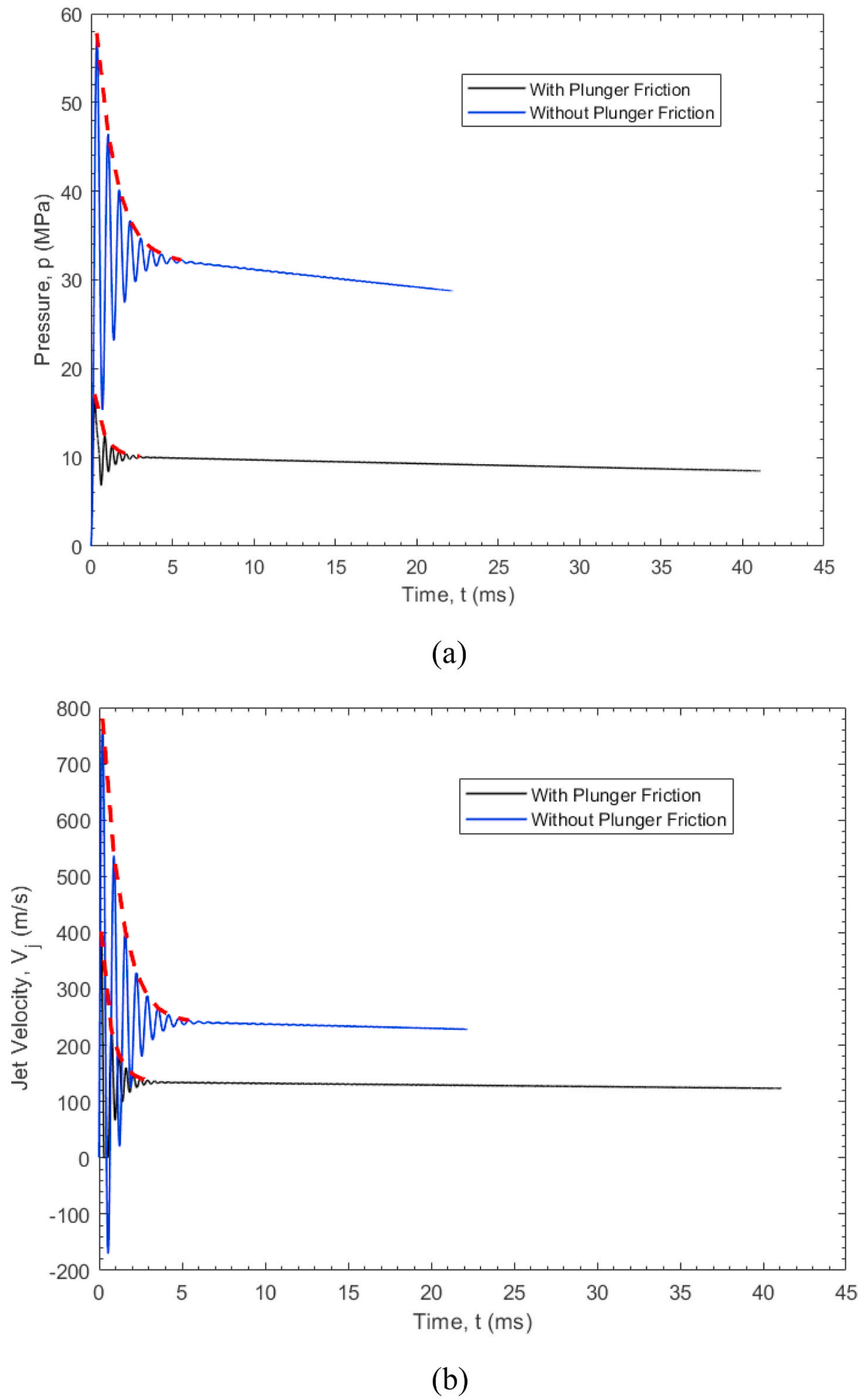


**Fig. 7.** (a) Comparison of cartridge pressure profiles using predictive model, (b) Comparison of jet velocity profile using predictive model (equation (8)). Fluid – Water, Cartridge geometry – ID pen (orifice diameter $d_0 = 157\ \mu$m). Red curves track the oscillation peaks for each profile.

(ode45 in MATLAB). The initial conditions for starting the solution iterations are: 1 mm/s plunger velocity [12], zero cartridge pressure and initial plunger position at 0 m. The absolute error tolerance was set to $10^{-5}$. As per equation (5), the force from actuation source (spring) gets divided into three main parts i.e., 1) inertial force of accelerating fluid in the upstream cartridge region 2) force required to overcome the rubber plunger friction and 3) force required to create a liquid jet through narrow orifice and overcome viscous, turbulence losses. To gain deeper understanding of the force balance, we will separately study the effects of plunger friction and fluid flow losses.

#### 3.2.1. *Effects of plunger frictional forces*

The rubber plunger tip acts as a moving barrier to hold liquid inside the cartridge during jet injection process. There are two main types of

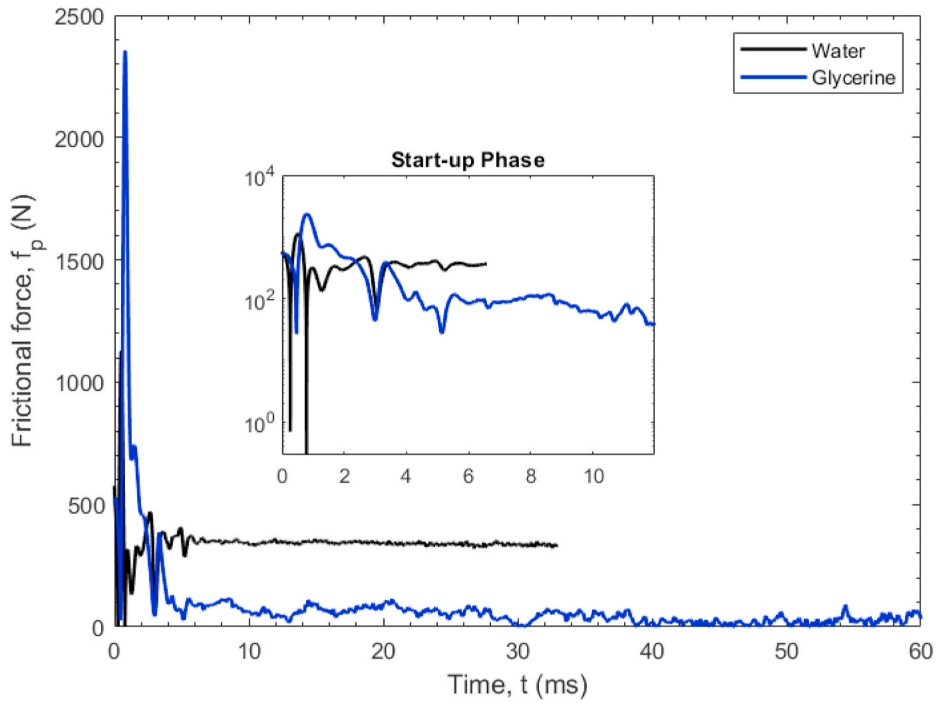


**Fig. 8.** Frictional force magnitude comparison for water and glycerine. For steady jet phase, the plunger frictional force is computed by subtracting pressure force (CFD pressure profile) from spring driving force. Note that force indicates magnitude only, not direction. Subplot shows the comparison on logarithmic y-axis. Geometry: ID pen.

frictional forces such as static friction (or break-loose force) and kinetic/gliding friction. According to the manufacturer, Bioject® ID pen uses nitrile rubber plunger material coated with silicone. The siliconization [31] of plunger tip helps reduce the kinetic friction but has tendency to increase the break-loose force over a long storage duration. To reduce this static friction, it is recommended to move the plunger before the initiating the jet injection process.

To gain insights into effects of plunger friction, we can consider a hypothetical scenario, where jet injection occurs without plunger frictional force and compute pressure and jet velocity profiles using the predictive model. From Fig. 7(a) & (b) we see that plunger friction reduces the initial oscillations in pressure and jet velocity. Increased

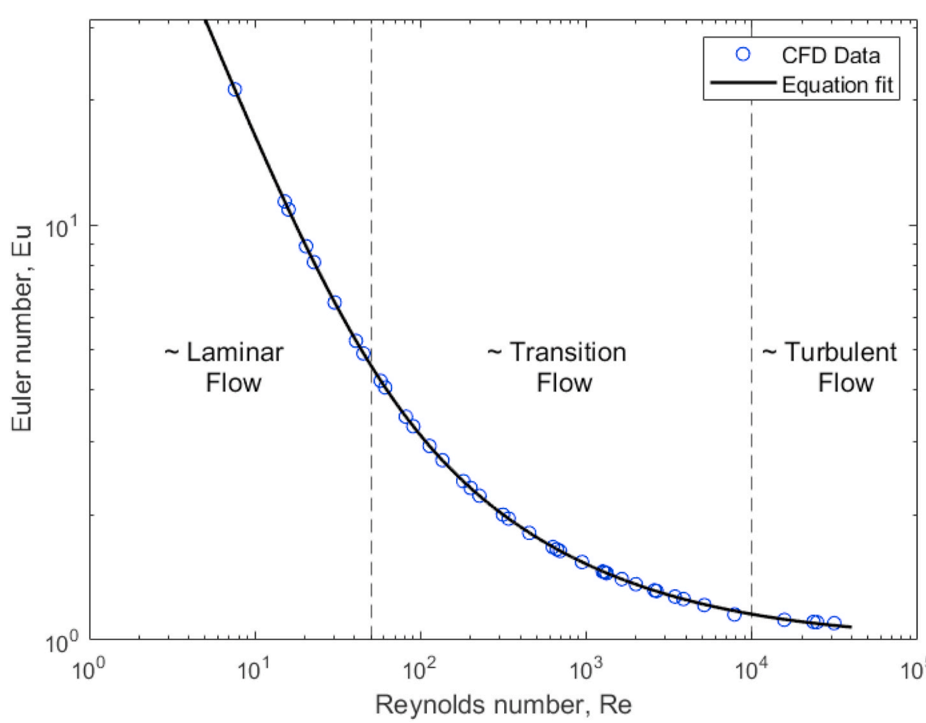


**Fig. 9.** Euler number ($Eu = \frac{p}{0.5\rho v_j^2}$) versus Reynolds number ($Re = \frac{\rho v_j d_o}{\mu}$) for ID pen geometry. In steady-state CFD simulations, the variation in Reynolds number was achieved by changing fluid viscosity and jet velocity. The black line represents the best empirical fit using equation (9) with parameters: q = 149.9, a = 4.6 × $10^{-3}$, b = 1.253, c = 0.3782.

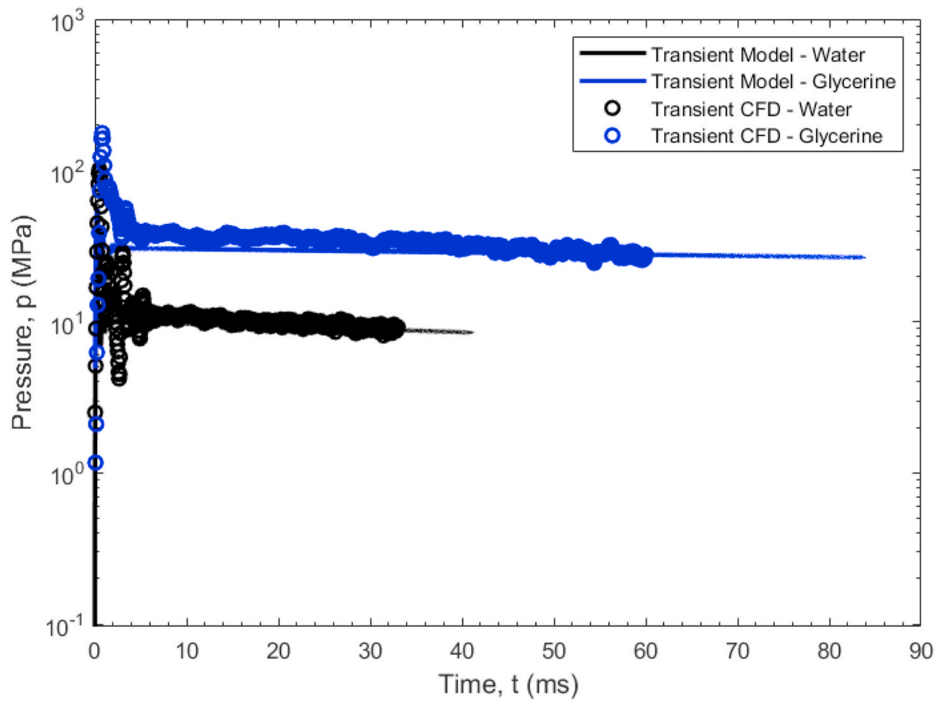


(a)

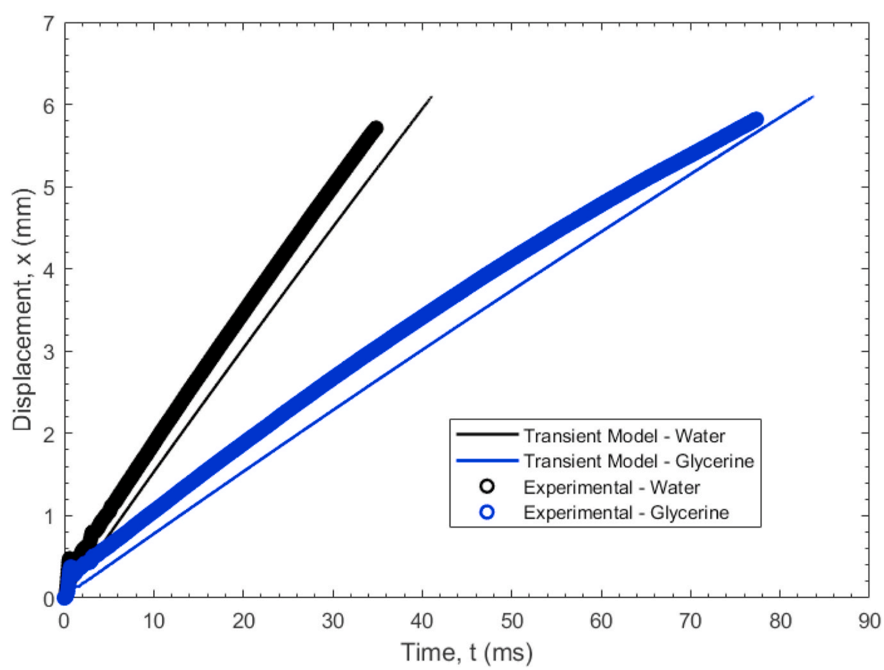


(b)

**Fig. 10.** (a) Comparison of pressure profiles generated from transient predictive model and transient CFD analysis (as per Fig. 6(b)) (b) Comparison of plunger displacement profiles generated from experiments and transient predictive model. Cartridge geometry: ID pen.

oscillations due to the absence of plunger friction can be likened to an underdamped system with an exponential decay [5,32,33]. Higher frictional forces will dampen oscillations at the expense of increasing pressure loss and injection time. Therefore, the plunger tip material and dimensions should be chosen such that the system is critically damped, where the time required to reach steady jet phase is lowest with minimal oscillations.

During the steady jet phase, Fig. 7(a) & (b) show a 70% reduction in cartridge pressure and 46% reduction in jet velocity due to plunger friction. Since tissue penetration depth decreases with jet velocity [14, 34–36], it is therefore important to estimate plunger friction before designing the jet injector system. The peak cartridge pressure showed a more than three-fold increase to 58 MPa in the absence of plunger friction, which would increase the required strength and thickness of cartridge walls to sustain such high stresses.

During the steady jet phase, the jet velocity profiles in Fig. 6(a) show approximately zero plunger acceleration, and thus zero net force acting on the plunger. Therefore, for a given actuation source (e.g. fixed spring constant), the cartridge pressure profile mainly depends on the plunger frictional force. Here, for the steady jet phase, we can calculate the plunger frictional force by subtracting the fluid pressure force (computed using CFD, Fig. 6(b)) from the spring driving force (equation (5)). Equations (6) and (7) can be further used to determine the coefficient of friction for water and glycerine, given as 0.5 and 0.01, respectively. As shown in Fig. 8, the averaged plunger frictional force for the case of water (~350 N) is approximately ten times that for glycerine (~35 N).

Previous studies [24,25,32] on predictive modelling of needle-free jet injectors do not entirely illustrate the major contributing factor in the effect of liquid properties on plunger friction. Literature [37–39] on tribology has shown that coefficient of friction differs with dry or lubricated environments as well as viscosity of a liquid. The difference between dry and lubricated coefficient of friction is due to the formation of a liquid film in the gap between the rubber plunger tip and cartridge walls. Low viscosity liquid can easily get squeezed out of the gap between plunger tip and walls upon plunger movement and high-pressure environment, resulting in higher friction coefficient for water as compared to glycerine.

### 3.2.2. Effects of viscous and turbulence losses

In the present study, the Euler number in equation (8) accounts for viscous and turbulence losses. Euler number is a dimensionless pressure which, here, physically represents the ratio of pressure energy used to jet kinetic energy produced. At $Eu = 1$, upstream static pressure energy is completely converted into downstream fluid velocity without any turbulence or viscous losses in fluid flow i.e., inviscid flow. Euler number has an inverse square relationship with the orifice discharge coefficient $\left(Eu = \frac{1}{C_d{}^2}\right)$, where the orifice discharge coefficient is a ratio of experimental flow rate to ideal theoretical flow rate through the orifice. A previous study [40] of pressure losses in microneedles used equation (9) and numerical modelling data to correlate Reynolds number to Euler number.

$$Eu = 1 + \left(\frac{q}{Re}\right)^{*}\left(1 + a^{*}Re^{b}\right)^{c} \tag{9}$$

Where, $q$, $a$, $b$, $c$ are constants for a particular cartridge geometry. In Fig. 9, the non-linear curve of equation (9) was fitted to the steady-state CFD simulations data with SSE ≈0.0011 and $R^2 \approx 1$. From Fig. 9, we can see that the Euler number gradually asymptotes towards unity as the Reynolds number increases. Equation (9) ensures that Euler number is above unity for all values of Reynolds number, especially in turbulent flow regime. For data fitting in the laminar flow regime (Re below ~ 50), equation (9) contains the term $\left(\frac{q}{Re}\right)$, where $q$ determines the steepness of decline in Euler number. Additionally, the accurate transition from laminar flow to turbulent flow can be modelled by regressing constants $a$, $b$ and, $c$ in the term $(1 + a^{*}Re^{b})^{c}$. Here, to satisfy the practical constraint of declining Euler number with increasing Reynolds number, the constants $b$ and $c$ can be varied for different cartridge geometries such that $bc < 1$.

By merging equations (8) and (9), we can express jet velocity ($v_j(t)$) as a function of geometry-specific Eu–Re correlation. With the inclusion of geometry-specific Eu–Re correlations in governing set of PDEs in transient predictive model (equations (4) and (5)), we can estimate the pressure losses and jet velocity for a wide variety of fluid viscosity for a given cartridge geometry. Note that this work can also be applied to non-Newtonian fluid rheology by generating correlations between Euler number versus generalized Reynolds number [7] for various cartridge geometries.

The modified equation (8) for ID pen cartridge geometry and Newtonian fluids can be written as follows:

$$v_j(t) = \sqrt{\frac{2p(t)}{\rho^{*}\left(1 + \left(\frac{149.9}{Re}\right)^{*}(1 + 0.004603^{*}Re^{1.253})^{0.3782}\right)}} \tag{10}$$

After incorporating equations (6), (7) and (10) into governing differential equations (4) and (5), we can accurately estimate the pressure and plunger displacement profile for ID pen cartridge geometry. Equation (10) is an implicit equation ($Re = \frac{\rho v_j d_o}{\mu}$) and thus, the set of governing differential equations can be iteratively solved using appropriate initial conditions.

In Fig. 10 (a), the transient CFD analysis shows an increase in the peak pressure from 101.4 MPa to 177.8 MPa, when the fluid changes from water to glycerine. We can rationalize this by recalling that the frictional forces associated with the plunger are lower for glycerine than water; As such, for the same applied spring force, reduction in the plunger frictional force causes an increase in net forward force applied to the liquid. Therefore, we see an increase in the peak fluid pressure for glycerine as compared to water. Although there is a higher net forward force in the case of glycerine, peak plunger displacement is lower than that for water (as shown in inset plot of Fig. 6(a)). This is due to the higher bulk modulus (or lower compressibility) value of glycerine, which resists the compressive downward plunger movement, even at higher peak pressures.

As per Fig. 9, there is a rapid decline of Euler number from $Eu$ ~20 to $Eu$ ~3 for $1 < \mathrm{Re} < 100$ followed by slow decline from $Eu$ ~3 to $Eu$ ~1.09 for $100 < \mathrm{Re} < 35000$. As the Reynolds number increases, the fluid flow gradually approaches inviscid flow. This suggests that operating in turbulent flow regime (at the orifice region) is beneficial to achieve higher energy efficiency. Fig. 10(a) certainly validates this since the averaged cartridge pressure (in the steady jet phase) for water (9.3 MPa) is 67% less than that of glycerine (30.3 MPa), yet the resulting jet velocities are 134 m/s and 63 m/s, respectively.

In steady-jet phase, the pressure profiles from CFD data matches with the pressure profiles from predictive model with an error less than 5% for both fluids. Using the predictive model, water shows a higher jet velocity (128.4 m/s) than glycerine (62.86 m/s), which compares favourably to the experimentally-determined jet velocities for both the liquids with less than 3% error.

However, the predictive model underestimates the plunger displacement throughout the jet injection period as seen in Fig. 10(b). Using the predictive model, we see the increase in peak pressure from 15.7 MPa to 58 MPa, when the fluid changes from water to glycerine. In experimental trials, we observe the plunger slippage in the first few oscillations in start-up phase, which may be attributed to slight expansion of the plastic cartridge and compression of the rubber plunger tip due to the sudden shock. In contrast, the predictive model does not allow for compliance of the plastic cartridge walls. This results in an underprediction of the plunger displacement even though the jet velocity (or plunger velocity) is accurately estimated.

Similarly, the transient CFD model does not consider the effects of cartridge expansion. Thus, using the experimental plunger displacement as an input to the transient CFD analysis results in overestimation of the peak pressures inside the cartridge. This limitation of the present study can be addressed in the future by developing a complex CFD model of system coupling with the two-way fluid structure interactions. However, our predictive approach provides a simple way to accurately estimate the jet velocity and cartridge pressure during the steady-jet phase, which is very useful in the industrial environment to rapidly develop a tailored cartridge geometry for a particular fluid.

In summary, we use the transient CFD analysis to estimate the pressure profile based upon the experimental plunger displacement

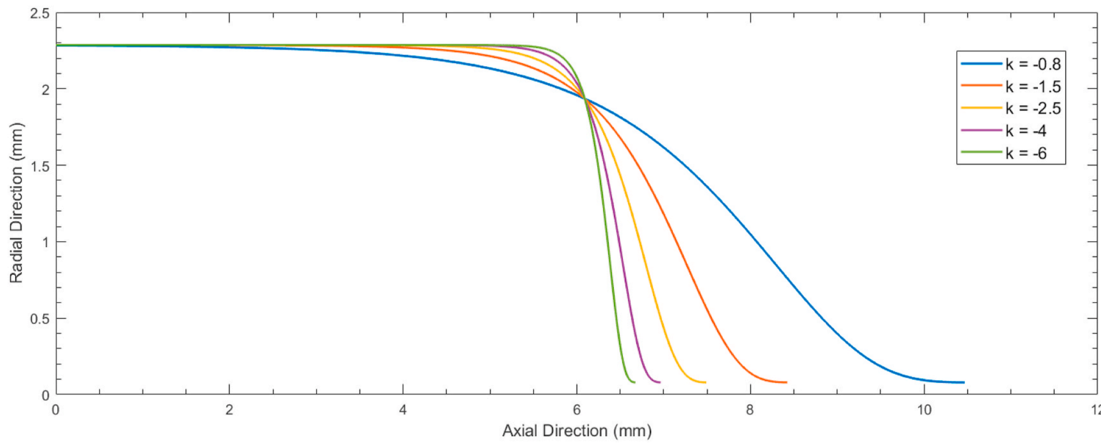


**Fig. 11.** Different geometry outlines obtained from Richard's function (equation (3)) at $\delta = 0.9$. Cartridge volume = 0.1 ml. Note the difference in scales for the axes. Upstream cartridge diameter (4.57 mm) and orifice diameter (155 µm) are kept the same for all cartridge geometries, including ID pen cartridge geometry.

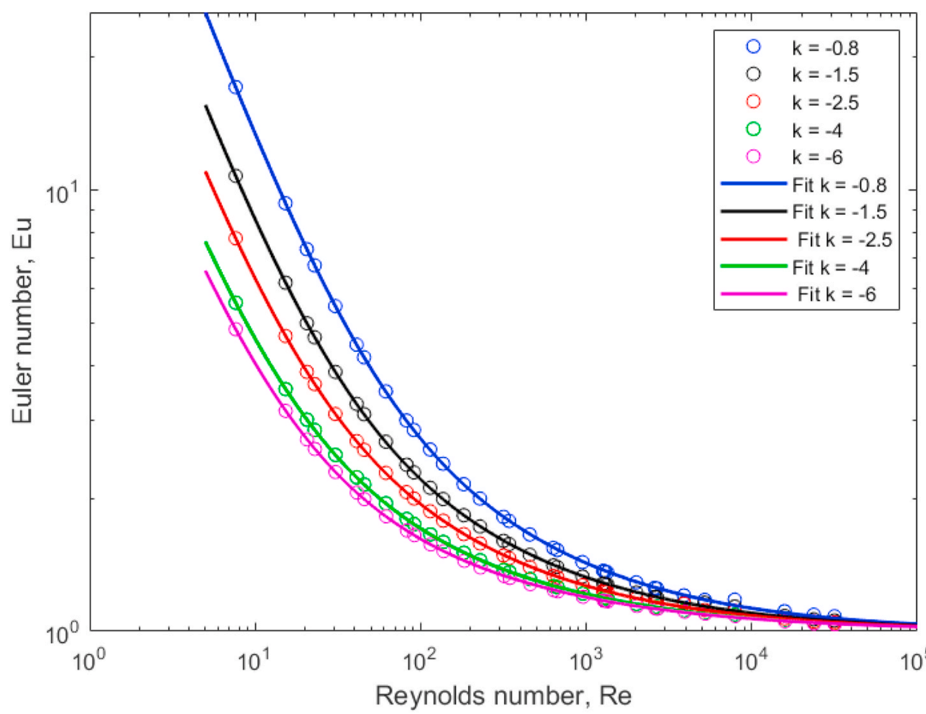


**Fig. 12.** Euler number (*Eu*) versus Reynolds number (Re) for cartridge geometries from Richard's function. *Eu* vs Re data from steady-state CFD simulations is represented as circular data points. In steady-state CFD simulations, the variation in Reynolds number was achieved by changing fluid viscosity and jet velocity.

profile and the steady state CFD simulations to generate characteristic curves of Euler number versus Reynolds number for each cartridge geometry. Resulting in an improved transient predictive model, which uses the characteristic curves (*Eu* vs. Re) to consider the effect of fluid viscosity and cartridge geometry and to accurately estimate the pressure and jet velocity profiles.

### 3.2.3. *Effect of variation in cartridge geometry*

In our previous work [7], we used an asymmetric sigmoid taper cartridge geometry given by Richard's function (equation (3)). In equation (3), variation in $k$ changes the incline for transition from plunger diameter to orifice diameter and variation in $\delta$ changes the length of a cartridge in the orifice region. For practical purposes of designing cartridge geometries, the orifice length can be fixed while achieving various cartridge tapers by variation of $k$ only, as per Fig. 11.

Using steady-state CFD data, we generate a characteristic curve of Euler number versus Reynolds number for each separate cartridge geometry. From Fig. 12, in the laminar flow regime (at Re ~ 10), there is significant effect of geometrical variation on Euler number, resulting in around 72% reduction in Euler number as we go from $k = -0.8$ to $k = -6$. Whereas we see very small (4%) decrease in Euler number for the same geometries as the flow approaches inviscid limit ($Re > 10^4$). Note that geometry outlines in Fig. 11 represent a range of sigmoidal contractions, all of which are smooth, but appear sharper for lower values of k due to the scales used. As such, we can rationalize the improved efficiency (lower *Eu*) in the low-Re regime by considering the growth of the boundary layer, which is more pronounced for smaller k values since these geometries have larger effective orifice lengths.

Thus, changing the cartridge geometry for low viscosity fluids such as water (Re ~ $O(10$ [4])) would result in negligible change in cartridge pressure profile or jet velocity profile. In other words, cartridge geometry is important for high-viscosity fluids, but less so for low-viscosity

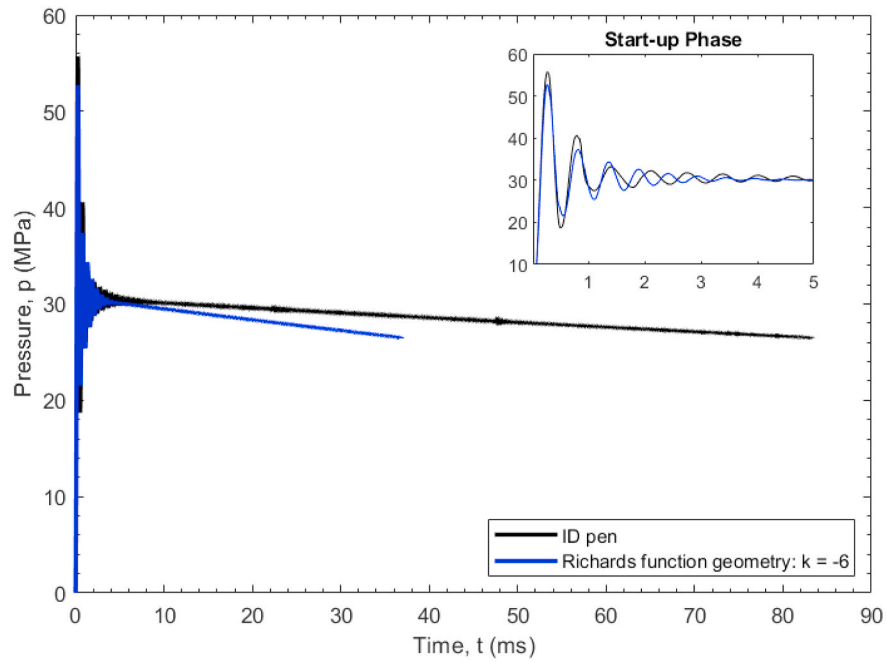


(a)

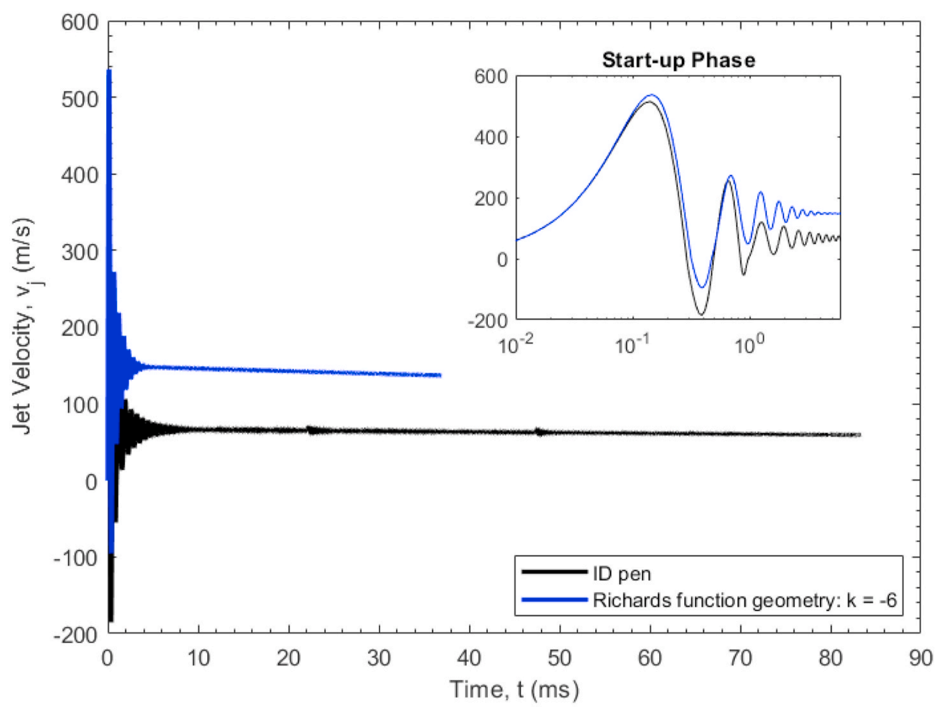


(b)

**Fig. 13.** Comparison between ID pen cartridge geometry and Richard's function cartridge geometry (k = −6, $\delta$ = 0.9). Orifice diameter for both geometries ($d_o$) = 155 μm. Fluid: Glycerine (Fluid properties as per Table 1). (a) pressure profiles generated using transient predictive model (b) Jet velocity profiles generated using transient predictive model.

fluids.

For a high viscosity fluid such as glycerine, the cartridge geometry has a significant impact on the pressure and jet velocity profiles as per Fig. 13(a) & (b). At $k = -6$, a sigmoid cartridge from Richard's function has slightly lower peak pressure (52.9 MPa) as compared to the ID pen cartridge (55.9 MPa).

Fig. 13 (b) shows that a sigmoid taper ($k = -6$) is more energy efficient than the ID pen geometry and therefore jet velocity increased by 128% from 62.8 m/s (Re ~ 15 at the orifice) to 143.6 m/s (Re ~ 35 at the orifice) for similar cartridge pressure (Fig. 13 (a)). Energy efficiency of a cartridge geometry also affects the time duration of initial oscillations (start-up phase) in the system. For the sigmoid taper (k = −6), the

**Table 3**
Parameters (in equation (9)) for correlation of Euler number to Reynolds number for cartridge geometries obtained from Richard's function. These parameters can be incorporated into equation (9) to generate *Eu* vs. Re curves as shown in Fig. 12.

| Richard Parameter '*k*' | *a* | *b* | *c* | *q* |
|---|---|---|---|---|
| −0.8 | 0.007691 | 1.129 | 0.4285 | 119.1 |
| −1.5 | 0.01408 | 1.119 | 0.438 | 70.44 |
| −2.5 | 0.02248 | 1.097 | 0.4555 | 47.4 |
| −4 | 0.03847 | 1.027 | 0.5072 | 30.29 |
| −6 | 0.0478 | 0.9594 | 0.57 | 24.82 |

start-up phase lasts around 4.5 ms, compared to about 9 ms for the ID pen cartridge.

The parameters *q*, *a*, *b*, and *c* show either a continuous increase or decrease with variation in *k* (as per Table 3). To expand the practical applicability of our primary predictive model, we have used secondary modelling, widely used in predictive microbiology literature [41,42], to express the parameters *q*, *a*, *b*, and *c* in terms of *k* in Richard's function. This analysis can then be used to determine Euler number for a particular Reynolds number for cartridge geometries with all *k* values within the ranges studied here.

From Table 3, we see that *q* decreased by almost 80% when *k* changes from −0.8 to −6. As discussed in section 3.2.2., *q* represents the steepness of decline in Euler number in laminar flow regime. At $k = -0.8$, a higher value of *q* signifies the drastic difference in Euler number from laminar regime to turbulent regime. Therefore, parameter *q* is directly proportional to the pressure losses in laminar flow regime for all cartridge geometries. Using an interpolation (supplementary info) technique, we can further expand the applicability of our predictive model. In principle, this means we could choose any Richards function parameter *k* (within the given range) and iteratively solve our model for different fluid rheology to accurately predict the jet injection behavior.

## 4. Conclusions

We have conducted a combined experimental-analytical-numerical investigation to study impact-driven NFJI. The first step in designing a needle-free jet injector is to identify the target tissue (e.g., intradermal, intramuscular, etc.) and estimate the required jet velocity and diameter to achieve that target penetration depth. These, together with the volume, guide the design of the cartridge and thus the required driving pressure. Therefore, for device manufacturing, it is important to rapidly and accurately estimate the cartridge pressure and jet velocities to ensure devices can achieve the correct operational conditions and reach the target tissue. In addition, it is deemed important to assess whether cartridge geometries can be tailored to fluid rheology for a specified jet injector power (actuation source power).

In the present study, we first derived the experimental plunger displacement using high-speed videography and performed numerical simulations to calculate cartridge pressure profiles. By developing empirical correlations for the jet Reynolds number and pressure loss in a cartridge, we expand the applicability of the existing predictive model to a wide variety of Newtonian and non-Newtonian fluids, where the apparent viscosity for a non-Newtonian fluid can be considered using the generalized Reynolds number. We observe that fluid viscosity and cartridge-plunger friction are the two most important considerations in tailoring the operation for certain tissue penetration depth. The results shows that the effect of cartridge geometry variation is significant in laminar flow regime. Depending on the drug rheology and resultant flow regime, manufacturers can decide whether it is important to tailor the cartridge geometry (fluid domain, cartridge thickness) to the specific drug.

Using empirical correlations to estimate the pressure losses for a cartridge geometry, we improve the applicability of an existing model to accurately predict the hydrodynamics of the process. The predictive model can reliably calculate the jet velocity with variation in fluid viscosity, cartridge geometry within the range of parameters studied here, and can be used to guide the design of future jet injectors.

## Acknowledgement

The jet injector device and cartridge were provided by Inovio Pharmaceuticals. This work was financially supported by National Science Foundation via award number NSF-CBET-1749382.

## Appendix A. Supplementary data

Supplementary data to this article can be found online at https://doi.org/10.1016/j.compbiomed.2021.104586.

## References

[1] M. Mercuri, D.F. Rivas, Challenges and opportunities for small volumes delivery into the skin, Biomicrofluidics 15 (2021).
[2] S. Mitragotri, Devices for overcoming biological barriers: the use of physical forces to disrupt the barriers, Adv. Drug Deliv. Rev. 65 (2013) 100–103.
[3] S. Coppola, V. Vespini, G. Nasti, P. Ferraro, Transmitting light through biocompatible and biodegradable drug delivery micro needles, IEEE J. Sel. Top. Quant. Electron. 27 (2021) 1–8.
[4] R. Vecchione, et al., Electro-drawn drug-loaded biodegradable polymer microneedles as a viable route to hypodermic injection, Adv. Funct. Mater. 24 (2014) 3515–3523.
[5] R. Portaro, H.D. Ng, Experiments and modeling of air-powered needle-free liquid injectors, J. Med. Biol. Eng. 35 (2015) 685–695.
[6] H. Nakayama, R. Portaro, C.B. Kiyanda, H.D. Ng, CFD modeling of high speed liquid jets from an air-powered needle-free injection system, J. Mech. Med. Biol. 16 (2016) 1650045.
[7] Y.S. Rane, J.O. Marston, Computational study of fluid flow in tapered orifices for needle-free injectors, J. Contr. Release 319 (2020) 382–396.
[8] J.A. Simmons, et al., Characterization of skin blebs from intradermal jet injection: ex-vivo studies, J. Contr. Release 307 (2019) 200–210.
[9] P. Rohilla, et al., Characterization of jets for impulsively-started needle-free jet injectors: influence of fluid properties, J. Drug Deliv. Sci. Technol. 53 (2019) 101167.
[10] N. Takagaki, et al., Estimation of high-speed liquid-jet velocity using a pyro jet injector, Sci. Rep. 9 (2019) 1–11.
[11] H. Miyazaki, S. Atobe, T. Suzuki, H. Iga, K. Terai, Development of pyro-drive jet injector with controllable jet pressure, J. Pharmacol. Sci. 108 (2019) 2415–2420.
[12] A.B. Baker, J.E. Sanders, Fluid mechanics analysis of a spring-loaded jet injector, IEEE Trans. Biomed. Eng. 46 (1999) 235–242.
[13] Technical considerations for pen, jet, and related injectors intended for use with drugs and biological products: guidance for industry and FDA staff. https://www.fda.gov/regulatory-information/search-fda-guidance-documents/technical-considerations-pen-jet-and-related-injectors-intended-use-drugs-and-biological-products, 2013.
[14] J. Seok, et al., Investigating skin penetration depth and shape following needle-free injection at different pressures: a cadaveric study, Laser Surg. Med. 48 (2016) 624–628.
[15] A.M. Römgens, et al., Penetration and delivery characteristics of repetitive microjet injection into the skin, J. Contr. Release 234 (2016) 98–103.
[16] P. Rohilla, J.O. Marston, In-vitro studies of jet injections, Int. J. Pharm. 568 (2019) 118503.
[17] W. Seehanam, K. Pianthong, W. Sittiwong, B. Milton, Injection pressure and velocity of impact-driven liquid jets, Eng. Comput. 31 (2014) 1130–1150.
[18] S. Mitragotri, Current status and future prospects of needle-free liquid jet injectors, Nat. Rev. Drug Discov. 5 (2006) 543–548.
[19] J. Baxter, S. Mitragotri, Needle-free liquid jet injections: mechanisms and applications, Expet Rev. Med. Dev. 3 (2006) 565–574.
[20] M. Moradiafrapoli, J.O. Marston, High-speed video investigation of jet dynamics from narrow orifices for needle-free injection, Chem. Eng. Res. Des. 117 (2017) 110–121.
[21] U.K. Griffiths, A.C. Santos, N. Nundy, E. Jacoby, D. Matthias, Incremental costs of introducing jet injection technology for delivery of routine childhood vaccinations: comparative analysis from Brazil, India, and South Africa, Vaccine 29 (2011) 969–975.
[22] A. Mohizin, K.E.R. Roy, D. Lee, S.K. Lee, J.K. Kim, Computational fluid dynamics of impinging microjet for a needle-free skin scar treatment system, Comput. Biol. Med. 101 (2018) 61–69.
[23] K. Chen, H. Zhou, An experimental study and model validation of pressure in liquid needle-free injection, Int. J. Phys. Sci. 6 (2011) 1552–1562.
[24] D. Zeng, et al., A mathematical model and experimental verification of optimal nozzle diameter in needle-free injection, J. Pharmacol. Sci. 107 (2018) 1086–1094.
[25] A. Mohizin, J.K. Kim, Effect of geometrical parameters on the fluid dynamics of air-powered needle-free jet injectors, Comput. Biol. Med. 118 (2020) 103642.

[26] W. Seehanam, K. Pianthong, W. Sittiwong, B.E. Milton, K. Takayama, Investigation on the generation process of impact-driven high-speed liquid jets using a CFD technique, Shock Waves 22 (2012) 465–475.
[27] J. Schramm, S. Mitragotri, Transdermal drug delivery by jet injectors: energetics of jet formation and penetration, Pharm. Res. (N. Y.) 19 (2002) 1673–1679.
[28] D. Zeng, N. Wu, L. Xie, X. Xia, Y. Kang, An experimental study of a spring-loaded needle-free injector: influence of the ejection volume and injector orifice diameter, J. Mech. Sci. Technol. 33 (2019) 5581–5588.
[29] E.O. Ogunti, O.R. Popoola, Fluid mechanics analysis of a voice coil needle free jet injector, Adv. Phys. Theor. Appl. 34 (2014) 60–69.
[30] J. Baxter, S. Mitragotri, Jet-induced skin puncture and its impact on needle-free jet injections: experimental studies and a predictive model, J. Contr. Release 106 (2005) 361–373.
[31] B. Reuter, C. Petersen, Syringe Siliconization Trends, methods, analysis procedures, TechnoPharm 2 (2012) 238–244.
[32] R. Portaro, J. Sadek, H. Xu, H.D. Ng, Controlled release using gas detonation in needle-free liquid jet injections for drug delivery, Appl. Sci. 9 (2019) 2712.
[33] K. Chen, M. Pan, T. Liu, Design and analysis of a continuous split typed needle-free injection system for animal vaccination, Open Biomed. Eng. J. 11 (2017) 59–71.
[34] D. Zeng, N. Wu, L. Qian, H. Shi, Y. Kang, Experimental investigation on penetration performance of larger volume needle-free injection device, J. Mech. Sci. Technol. 34 (2020) 3897–3909.
[35] T.M. Grant, K.D. Stockwell, J.B. Morrison, D.D. Mann, Effect of injection pressure and fluid volume and density on the jet dispersion pattern of needle-free injection devices, Biosyst. Eng. 138 (2015) 59–64.
[36] J. Schramm-Baxter, S. Mitragotri, Needle-free jet injections: dependence of jet penetration and dispersion in the skin on jet power, J. Contr. Release 97 (2004) 527–535.
[37] S.H. Teoh, R. Thampuran, W.K.H. Seah, Coefficient of friction under dry and lubricated conditions of a fracture and wear resistant P/M titanium-graphite composite for biomedical applications, Wear 214 (1998) 237–244.
[38] L. Chen, et al., Surface characterization and tribological performance of anodizing micro-textured aluminum-silicon alloys, Materials 12 (2019).
[39] A.J. Tuononen, Onset of frictional sliding of rubber-glass contact under dry and lubricated conditions, Sci. Rep. 6 (2016) 1–10.
[40] W. Martanto, S.M. Baisch, E.A. Costner, M.R. Prausnitz, M.K. Smith, Fluid dynamics in conically tapered microneedles, AIChE J. 51 (2005) 1599–1607.
[41] H. Li, G. Xie, A.S. Edmondson, Review of secondary mathematical models of predictive microbiology, J. Food Prod. Market. 14 (2008) 57–74.
[42] J. Ferrer, C. Prats, D. López, J. Vives-Rego, Mathematical modelling methodologies in predictive food microbiology: a SWOT analysis, Int. J. Food Microbiol. (2009) 134 2–8.